

Grain orientation, texture, and internal stress optically evaluated by micro-Raman spectroscopy

M. Becker^{a)} and H. Scheel^{b)}

Universität Erlangen-Nürnberg, Institut für Werkstoffwissenschaften, Lehrstuhl Mikrocharakterisierung, Cauerstraße 6, 91058 Erlangen, Germany

S. Christiansen

Martin-Luther-Universität Halle-Wittenberg, Hoher Weg 8, 06120 Halle, Germany

H. P. Strunk

Universität Erlangen-Nürnberg, Institut für Werkstoffwissenschaften, Lehrstuhl Mikrocharakterisierung, Cauerstraße 6, 91058 Erlangen, Germany

(Received 21 September 2006; accepted 6 December 2006; published online 27 March 2007)

We present a method to experimentally determine the components of stress tensors within grains of multicrystalline materials by micro-Raman spectroscopy. This method is applied to multicrystalline silicon wafers as they are produced for solar cells. Currently, μ -Raman spectroscopy is intensively used to measure stresses in silicon wafers, structures, and devices of known crystallographic orientations. For these cases, the determination of stresses from Raman peak shifts is straightforward. In multicrystalline silicon, however, arbitrary grain orientations complicate the determination of stress tensor components, which depend on the crystallographic orientations of the particular grains. The Raman intensities depend on the polarization direction of the incident and scattered laser light and again on the crystallographic grain orientations. This intensity dependence is used to determine the crystallographic grain orientations. Once the orientation is determined, the components of the stress tensor (with respect to a fixed reference coordinate system—the sample stage), can be calculated numerically from the Raman peak shifts. As examples, we determine (i) the stress components of a nearly plane stress state around the tip of a microcrack and (ii) the stress components at a grain boundary in a multicrystalline silicon wafer.

© 2007 American Institute of Physics. [DOI: [10.1063/1.2434961](https://doi.org/10.1063/1.2434961)]

I. INTRODUCTION

μ -Raman spectroscopy is a method that is used recently in solid state physics to investigate mechanical stresses in semiconductor materials.^{1–4} μ -Raman spectroscopy detects strains and stresses in crystals via an inelastic interaction of laser light with lattice vibrations (phonons). The method probes the material of interest nondestructively without requiring any complex sample preparations. μ -Raman spectroscopy allows for a lateral resolution of the order of $\sim 600\text{ nm} - 1\text{ }\mu\text{m}$ when focusing the incident light beam through optical elements (lenses) on the sample surface. Raman signals can be mapped and respective stress mappings can be determined.⁵ Meanwhile, the determination of several stress-tensor components in crystals with diamond structure have already been shown.^{6–10} But the stress/strain analysis has been carried out only for monocrystalline samples with known orientation. Similar stress-tensor determination have not been shown for polycrystalline materials with diamond structure, e.g., polycrystalline silicon wafers for solar cells or thin film transistors¹¹ (TFTs) due to the fact that grain orientation variations make stress measurements increasingly dif-

ficult. In the present article we show how to measure several stress-tensor components with μ -Raman spectroscopy in polycrystalline silicon within grains of arbitrary orientations. A single measurement cycle provides the local determination of orientation and stress/strain tensor components when making use of polarized incident light and detection of the polarization of the scattered light. Examples of practical interest of polycrystalline photovoltaic silicon material are given.

II. THEORETICAL BACKGROUND

The evaluation of stress-tensor components in silicon grains of arbitrary orientation can be divided into three steps: (i) The grain orientations have to be determined with respect to a fixed coordinate system. We use the x - y sample stage and as z direction the direction of the exciting laser beam; (ii) the Raman peak shifts have to be determined while taking into account the knowledge of the grain orientations; and (iii) the mathematical procedures to determine stress tensor components have to be adapted to arbitrary grain orientations.

A. Orientation measurements

The Raman peak intensities depend on the polarization vectors of the incident and scattered beams, \vec{e}_i , \vec{e}_s , respectively, which are defined in the fixed reference coordinate system. Raman intensities and polarization vectors are connected by the so-called Raman tensors.¹² As silicon belongs

^{a)}Present address: Martin-Luther-Universität Halle-Wittenberg, Hoher Weg 8, 06120 Halle, Germany.

^{b)}Present address: Universität Erlangen-Nürnberg, Institut für Werkstoffwissenschaften, Lehrstuhl Glas und Keramik, Martensstraße 5, 91058 Erlangen, Germany.

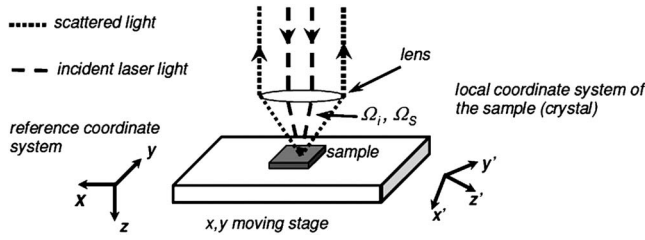


FIG. 1. Micro-Raman spectroscopy setup. The incident laser beam is focused by a lens on the sample surface and the scattered light is collected by the same lens. Ω_i and Ω_s are the angles for the cones of the incident and scattered light. The reference coordinate system remains fixed. All physical properties of the sample refer to the crystal coordinate system.

to the crystallographic O_h class, its Raman active optical phonons have F_{2g} symmetry and thus are triply degenerate in unstrained silicon. Each of the three optical phonons is represented by one Raman tensor \mathbf{R}'_j (Ref. 12) [in a crystal coordinate system that is oriented along the reference coordinate system: $x=x'=(100)$, $y=y'=(010)$, $z=z'=(001)$; see Fig. 1]:

$$\begin{aligned} \mathbf{R}'_x &= \begin{pmatrix} 0 & 0 & 0 \\ 0 & 0 & d \\ 0 & d & 0 \end{pmatrix}, \\ \mathbf{R}'_y &= \begin{pmatrix} 0 & 0 & d \\ 0 & 0 & 0 \\ d & 0 & 0 \end{pmatrix}, \\ \mathbf{R}'_z &= \begin{pmatrix} 0 & d & 0 \\ d & 0 & 0 \\ 0 & 0 & 0 \end{pmatrix}, \end{aligned} \quad (1)$$

with d representing a material constant that can be set to 1 for our purpose.

The scattered Raman intensity $I(\vec{e}_i, \vec{e}_s)$ after passing a lens with a small numerical aperture, e.g., a $10\times$ objective, can be sufficiently approximated by^{13,14}

$$I(\vec{e}_i, \vec{e}_s) \approx I_0 \cdot \sum_{j=1}^3 |\vec{e}_i \cdot \mathbf{R}'_j \cdot \vec{e}_s|^2, \quad (2)$$

with I_0 containing all fixed experimental parameters (laser intensity, laser wavelength, integration time, etc.). The index j discriminates the three phonon polarization directions x , y , z , and \vec{e}_i , \vec{e}_s are the polarization vectors of the incident

and scattered light, respectively. \mathbf{R}'_j represents the Raman tensors for the different phonon polarization directions. The three Raman tensors \mathbf{R}'_j (with $j=x, y, z$) refer to the crystal coordinate system of the considered grain and have to be transformed to the global reference coordinate system (sample stage) for arbitrary grain orientations, as \vec{e}_i and \vec{e}_s refer to the global reference coordinate system. The transformation is accomplished by applying a rotation matrix $\mathbf{T}(\alpha, \beta, \gamma)$, where α , β , and γ represent the three Euler angles. The explicit expression of $\mathbf{T}(\alpha, \beta, \gamma)$ is given in the Appendix.

Inserting the rotated Raman tensors \mathbf{R}_j into Eq. (2) the basic formula for the determination of the three Euler angles α , β , and γ from measurements of the Raman peak intensities is determined according to

$$I(\vec{e}_i, \vec{e}_s, \alpha, \beta, \gamma) \approx I_0 \cdot \sum_{j=1}^3 |\vec{e}_i \cdot (\mathbf{T}^{-1}(\alpha, \beta, \gamma) \cdot \mathbf{R}'_j \cdot \mathbf{T}(\alpha, \beta, \gamma)) \cdot \vec{e}_s|^2. \quad (3)$$

B. Strain/stress-measurements

The eigenfrequencies of optical phonons can in general be determined by solving the eigenvalue problem¹⁵

$$(\mathbf{K} - \omega^2 \cdot \mathbf{E}) \cdot \vec{q} = 0. \quad (4)$$

ω represents the eigenfrequencies (with or without strain), \vec{q} the eigenvectors. \mathbf{K} is the force constant tensor, the components of which are sensitive to strain, and \mathbf{E} is the identity matrix. For small strains, one may use a linear approximation for the components of \mathbf{K} (Ref. 15)

$$K_{ij} = K_{ij}^{(0)} + \sum_{kl} \varepsilon'_{kl} \cdot K_{ijkl}^{(\varepsilon')} \quad \text{with } K_{ij}^{(0)} = \omega_0^2 \cdot \delta_{ij} \quad \text{and} \quad K_{ijkl}^{(\varepsilon')} = \frac{\partial K_{ij}}{\partial \varepsilon'_{kl}}. \quad (5)$$

ε'_{kl} are the strain tensor components (in the crystal coordinate system), $K_{ijkl}^{(\varepsilon')}$ the phonon deformation potentials, and ω_0 is the phonon frequency without strain. Due to the cubic symmetry of silicon, the phonon deformation potential tensor $\mathbf{K}^{(\varepsilon')}$ has only three independent components¹⁵: p , q , and r .

Inserting Eq. (5) into Eq. (4) finally yields the secular equation¹⁵

$$\begin{vmatrix} p \cdot \varepsilon'_{xx} + q \cdot (\varepsilon'_{yy} + \varepsilon'_{zz}) - \lambda & 2r \cdot \varepsilon'_{xy} & 2r \cdot \varepsilon'_{xz} \\ 2r \cdot \varepsilon'_{xy} & p \cdot \varepsilon'_{yy} + q \cdot (\varepsilon'_{xx} + \varepsilon'_{zz}) - \lambda & 2r \cdot \varepsilon'_{yz} \\ 2r \cdot \varepsilon'_{xz} & 2r \cdot \varepsilon'_{yz} & p \cdot \varepsilon'_{zz} + q \cdot (\varepsilon'_{xx} + \varepsilon'_{yy}) - \lambda \end{vmatrix} = 0. \quad (6)$$

The eigenvalues λ_j represent the Raman frequency shifts in the presence of strain

$$\lambda_{1,2,3} = (\omega_{1,2,3}^2 - \omega_0^2) = (\omega_{1,2,3} - \omega_0) \cdot (\omega_{1,2,3} + \omega_0) \approx \Delta\omega_{1,2,3} \cdot 2\omega_0. \quad (7)$$

Equation (6) contains six unknown strain tensor components. The Raman shift measurements yield, however, three frequency shifts (three optical phonons) at most. Hence, not all six strain/stress tensor components can be determined from frequency shift measurements.

C. The stress state

Usually, in stress measurements using Raman spectroscopy, laser wavelengths that are absorbed close to the sample surfaces, are used. Thus only the stress distributions close to the sample surface can be determined, which represent nearly a plane stress state σ (small residual stress components in the z direction) with respect to the reference coordinate system

$$\sigma = \begin{pmatrix} \sigma_{xx} & \tau_{xy} & 0 \\ \tau_{xy} & \sigma_{yy} & 0 \\ 0 & 0 & \Delta_z \end{pmatrix}. \quad (8)$$

The component Δ_z comprehends the residual stress components σ_{zz} , τ_{xz} , and τ_{yz} . The Raman frequency shifts $\Delta\omega_{1,2,3}$ depend on the strain tensor components of the specific grains with their specific crystal coordinate systems. Therefore, the plane stress state σ , with respect to the reference coordinate system, has to be transformed into the specific crystal coordinate systems by the rotation matrix $T(\alpha, \beta, \gamma)$. This gives the transformed stress tensor σ'

$$\sigma' = \begin{pmatrix} \sigma'_{xx} & \tau'_{xy} & \tau'_{xz} \\ \tau'_{xy} & \sigma'_{yy} & \tau'_{yz} \\ \tau'_{xz} & \tau'_{yz} & \sigma'_{zz} \end{pmatrix} = T^{-1}(\alpha, \beta, \gamma) \cdot \sigma \cdot T(\alpha, \beta, \gamma). \quad (9)$$

Using the inverse Hooke's law (in vector notation) for cubic systems¹⁶

$$\begin{pmatrix} \varepsilon'_{xx} \\ \varepsilon'_{yy} \\ \varepsilon'_{zz} \\ \varepsilon'_{yz} \\ \varepsilon'_{xz} \\ \varepsilon'_{xy} \end{pmatrix} = \begin{pmatrix} S_{11} & S_{12} & S_{12} & 0 & 0 & 0 \\ S_{11} & S_{11} & S_{12} & 0 & 0 & 0 \\ S_{12} & S_{12} & S_{11} & 0 & 0 & 0 \\ 0 & 0 & 0 & S_{44} & 0 & 0 \\ 0 & 0 & 0 & 0 & S_{44} & 0 \\ 0 & 0 & 0 & 0 & 0 & S_{44} \end{pmatrix} \cdot \begin{pmatrix} \sigma'_{xx} \\ \sigma'_{yy} \\ \sigma'_{zz} \\ \sigma'_{yz} \\ \sigma'_{xz} \\ \sigma'_{xy} \end{pmatrix}, \quad (10)$$

we are able to express the strain tensor components ε'_{kl} in Eq. (6) by the stress tensor components σ'_{kl} . Using then Eq. (9), we may finally rewrite the secular Eq. (6) in terms of the stress components σ_{xx} , τ_{xy} , σ_{yy} , and Δ_z , with respect to the global (wafer) reference coordinate system

$$[\mathbf{A} \cdot \sigma_{xx} + \mathbf{B} \cdot \tau_{xy} + \mathbf{C} \cdot \sigma_{yy} + \mathbf{D} \cdot \Delta_z - \lambda \cdot \mathbf{E}] = 0, \quad (11a)$$

or explicitly

$$\begin{aligned} & \begin{pmatrix} A_{11} & A_{12} & A_{13} \\ A_{12} & A_{22} & A_{23} \\ A_{13} & A_{23} & A_{33} \end{pmatrix} \cdot \sigma_{xx} + \begin{pmatrix} B_{11} & B_{12} & B_{13} \\ B_{12} & B_{22} & B_{23} \\ B_{13} & B_{23} & B_{33} \end{pmatrix} \cdot \tau_{xy} \\ & + \begin{pmatrix} C_{11} & C_{12} & C_{13} \\ C_{12} & C_{22} & C_{23} \\ C_{13} & C_{23} & C_{33} \end{pmatrix} \cdot \sigma_{yy} + \begin{pmatrix} D_{11} & D_{12} & D_{13} \\ D_{12} & D_{22} & D_{23} \\ D_{13} & D_{23} & D_{33} \end{pmatrix} \cdot \Delta_z \\ & - \lambda \cdot \begin{pmatrix} 1 & 0 & 0 \\ 0 & 1 & 0 \\ 0 & 0 & 1 \end{pmatrix} = 0. \end{aligned} \quad (11b)$$

The components of the symmetric matrices \mathbf{A} , \mathbf{B} , \mathbf{C} , and \mathbf{D} depend on the elastic compliances S_{11} , S_{12} , and S_{44} for silicon, on the phonon deformation potentials for silicon p , q , and r and on the components of the rotation matrix $T(\alpha, \beta, \gamma)$. Therefore, all these components are constants for a particular grain. The secular Eq. (11a) and (11b) leads to the characteristic polynomial

$$P(\lambda) = \lambda^3 + a\lambda^2 + b\lambda + c. \quad (12)$$

The coefficients a , b , and c are functions of the stress components σ_{xx} , τ_{xy} , σ_{yy} , and Δ_z of the stress state with respect to the reference coordinate system. According to the rule of Vieta, we can find three equations for the (numerical) determination of the stress components σ_{xx} , τ_{xy} , σ_{yy} , and Δ_z from the Raman frequency shifts

$$a(\sigma_{xx}, \tau_{xy}, \sigma_{yy}, \Delta_z) = -2\omega_0(\Delta\omega_1 + \Delta\omega_2 + \Delta\omega_3),$$

$$b(\sigma_{xx}, \tau_{xy}, \sigma_{yy}, \Delta_z) = (2\omega_0)^2(\Delta\omega_1 \cdot \Delta\omega_2 + \Delta\omega_1 \cdot \Delta\omega_3 + \Delta\omega_2 \cdot \Delta\omega_3),$$

$$c(\sigma_{xx}, \tau_{xy}, \sigma_{yy}, \Delta_z) = -(2\omega_0)^3 \cdot (\Delta\omega_1 \cdot \Delta\omega_2 \cdot \Delta\omega_3). \quad (13)$$

The component Δ_x is used as an adjustment parameter, as we will see in Sec. III B. The coefficient a has a linear, coefficient b has a quadratic, and coefficient c has a cubic dependence on the stress components σ_{xx} , τ_{xy} , σ_{yy} , and Δ_z .

III. EXPERIMENTAL RESULTS AND DISCUSSION

Experimental Raman measurements are carried out using a *Jobin-Yvon LabramHR 800* microscope/spectroscopy. For the results presented in this article, we used the 633 nm emission line of the HeNe laser. The incident laser beam has a power of ≈ 10 mW on the sample surface. The attached microscope has four objective lenses: 100 \times (numerical aperture: 0.9), 50 \times (N.A.: 0.75), 10 \times (N.A.: 0.25), and a macro-objective. We performed the orientation measurements with the 10x objective (size of the focused spot on the sample surface was ≈ 10 μm in diameter) and the stress measurements with the 50x objective (size of the focused spot was ≈ 1.5 μm in diameter). The sample is mounted on a motorized x - y stage, which makes stress and/or orientation mappings possible. A notch filter eliminates the Rayleigh peak from the spectrum of the scattered light. A grating with 1800 lines/mm allows us to carry out spectra analysis of the scattered light. Using peak fitting routines, we are able to detect peak shifts with a resolution of $\sim \pm 0.05$ cm^{-1} . This

value results from (i) the error of the peak fitting routines and (ii) from the peak shift noise, which was determined by mapping a stress-free Si-wafer surface and analyzing the occurring peak-shift variations. The spectra are recorded with a silicon charge-coupled device (CCD) (1024×256 pixels) and can be displayed and processed on a PC.

As an example for the combined orientation and stress measurement procedures, we investigate (i) the stress distribution around the tip of a microcrack in an arbitrarily oriented grain of a multicrystalline solar silicon wafer (average grain size: $\approx 1 \text{ cm}^2$) and (ii) the stress distribution along an arbitrary large angle grain boundary. Prior to the measurements, the wafer has chemomechanically been polished. After polishing, the wafer has been Secco-etched¹⁷ for 10 s so that the grain boundaries can be distinguished in an optical microscope as small trenches. The surface normal of the wafer is the z axis of the reference coordinate system (the direction of the incident/scattered beam).

A. The orientation measurements

Equation (3) is the basis for orientation measurements using Raman spectroscopy. The polarization direction \vec{e}_i of the incident laser beam can be adjusted with a $\lambda/2$ plate. However, the influence of the mirrors and the notch-filter on the polarization direction of the incident beam after passing the $\lambda/2$ plate results in a dependence of the intensity of the incident laser beam on its polarization direction¹⁸ and a difference between the effective polarization direction ϕ on the sample surface and the original polarization direction $\tilde{\phi} = 2\theta$ that is adjusted with the $\lambda/2$ plate.¹⁸ We account for these deviations by introducing a correction factor k (the method used here is very similar to the method that is described in more details in Ref. 18). The polarization vector of the incident beam is then elliptically depending on the effective polarization direction ϕ and can be written as

$$\vec{e}_i = \begin{pmatrix} \cos \phi \\ k \cdot \sin \phi \\ 0 \end{pmatrix} \text{ with } 0 \leq k \leq 1 \text{ in our case.} \quad (14)$$

The intensity of the incident laser beam corresponds to the output current of a photodiode which is placed into the path of the incident beam. From the variations of the current of the photodiode with the position of the $\lambda/2$ plate, the correction factor k can be determined. In our case we obtain $k = 0.952$.

In a similar way, one may write for the effective polarization vector \vec{e}_s of the scattered beam

$$\vec{e}_s = \begin{pmatrix} m \cos \eta \\ \sin \eta \\ 0 \end{pmatrix}. \quad (15)$$

With η describing the analyzer position. The correction factor m accounts for the optical grating to modify the polarization direction of the scattered beam. The influence of the optical grating could also be eliminated by putting a $\lambda/4$ plate (scrambler) into the path of the scattered light. As we will see, the influence of the optical grating is of no impor-

tance for the determination of the crystallographic orientations. Therefore we will not go into further details here.

Inserting Eqs. (14) and (15) into Eq. (3) finally results in a concise matrix equation

$$I(\phi, \eta, \alpha, \beta, \gamma) \approx I_0 \cdot \begin{pmatrix} \cos^2 \phi \\ k \cdot \cos \phi \sin \phi \\ k^2 \cdot \sin^2 \phi \end{pmatrix}^T \cdot \begin{pmatrix} f_{11}(\alpha, \beta, \gamma) & f_{12}(\alpha, \beta, \gamma) & f_{13}(\alpha, \beta, \gamma) \\ f_{12}(\alpha, \beta, \gamma) & f_{22}(\alpha, \beta, \gamma) & f_{23}(\alpha, \beta, \gamma) \\ f_{13}(\alpha, \beta, \gamma) & f_{23}(\alpha, \beta, \gamma) & f_{33}(\alpha, \beta, \gamma) \end{pmatrix} \cdot \begin{pmatrix} m^2 \cdot \cos^2 \eta \\ m \cdot \cos \eta \sin \eta \\ \sin^2 \eta \end{pmatrix}. \quad (16)$$

The components $f_{ij}(\alpha, \beta, \gamma)$ of the symmetric matrix \mathbf{f} are trigonometric functions of the three Euler angles α , β , and γ and are given in the Appendix. For the two accessible analyzer positions ($\eta = 0^\circ$ and $\eta = 90^\circ$) Eq. (16) yields two ϕ -dependent intensity functions (short notation)

$$\begin{aligned} I_{\phi x} &= I(\phi, 0^\circ, \alpha, \beta, \gamma) \\ &= I_0 \cdot (f_{11} \cdot \cos^2 \phi + k \cdot f_{12} \cdot \cos \phi \sin \phi \\ &\quad + k^2 \cdot f_{13} \cdot \sin^2 \phi) \cdot m^2, \\ I_{\phi y} &= I(\phi, 90^\circ, \alpha, \beta, \gamma) \\ &= I_0 \cdot (f_{13} \cdot \cos^2 \phi + k \cdot f_{23} \cdot \cos \phi \sin \phi \\ &\quad + k^2 \cdot f_{33} \cdot \sin^2 \phi). \end{aligned} \quad (17)$$

To fit the experimental data, we therefore use the following two fit functions:

$$\begin{aligned} \text{Fit}_{\phi x} &= U_1 \cos^2 \phi + U_2 \cos \phi \sin \phi + U_3 \sin^2 \phi, \\ \text{Fit}_{\phi y} &= V_1 \cos^2 \phi + V_2 \cos \phi \sin \phi + V_3 \sin^2 \phi, \end{aligned} \quad (18)$$

with U_1 , U_2 , U_3 and V_1 , V_2 , V_3 being adjustable coefficients. Comparing fitted and calculated data from Eqs. (17) and (18) yield ratios $u_1 = U_1/U_3$, $u_2 = U_2/U_3$, $v_1 = V_1/V_3$, and $v_2 = V_2/V_3$ which lead to the final equation system we may use for the determination of the three Euler angles α , β , and γ by the Gauss-Newton method¹⁹

$$\begin{aligned} (k^2 \cdot u_1) \cdot f_{13}(\alpha, \beta, \gamma) - f_{11}(\alpha, \beta, \gamma) &= 0, \\ (k \cdot u_2) \cdot f_{13}(\alpha, \beta, \gamma) - f_{12}(\alpha, \beta, \gamma) &= 0, \\ (k^2 \cdot v_1) \cdot f_{33}(\alpha, \beta, \gamma) - f_{13}(\alpha, \beta, \gamma) &= 0, \\ (k \cdot v_2) \cdot f_{33}(\alpha, \beta, \gamma) - f_{23}(\alpha, \beta, \gamma) &= 0. \end{aligned} \quad (19)$$

The equation system (19) contains the correction factor k but not the correction factor m , i.e., the optical grating has no influence on the orientation measurements. The elimination of the scaling factor I_0 in Eq. (19) avoids repeated intensity calibration measurements prior to the orientation measurements. Thus, all the errors that may result from a change of

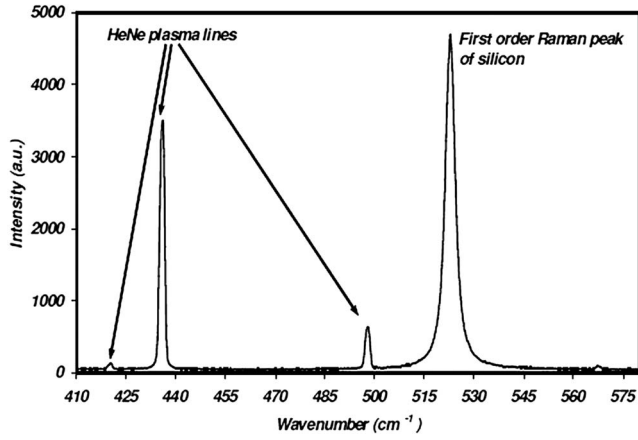


FIG. 2. Raman spectrum at an arbitrary position on our multicrystalline silicon wafer. In addition to the silicon Raman peak, the plasma lines of the HeNe laser are visible. The (physically defined) plasma line at $\approx 433 \text{ cm}^{-1}$ is used as a reference for frequency shift measurements of the silicon peak.

I_0 (e.g., due to an accidental change of experimental conditions during the measurements on different grains such as surface structure and/or dirt on the surface, a slight defocus, etc.) do not affect the orientation measurements.

The equation system (19) contains four equations for the numerical determination of the three Euler angles α , β , and γ , i.e., we cannot expect to find an exact solution of these equations. Instead, we use that set of Euler angles that gives the minimal norm of the numerical residual vector. Depending on the start values, the numerical iterative procedure used to solve equation system (19) gives several equivalent sets of Euler angles (within the periodicity rules of the Euler angles). These different sets of Euler angles lead to permutations of rows of the rotation matrix $\mathbf{T}(\alpha, \beta, \gamma)$. These permutations are a result of the ambiguity that exists in labeling the three axes of the cubic crystal coordinate system. Consequently, the designation of the three optical phonons and their frequency shifts will mutually interchange if equivalent sets of Euler angles are used to calculate the rotation matrix $\mathbf{T}(\alpha, \beta, \gamma)$. Finally, this will result in a change of stress tensors which refer to a certain crystal coordinate system, whereas the stress tensors referring to the global reference coordinate system will not change.

B. The stress measurements

Figure 2 shows a Raman spectrum that has been obtained at an arbitrary position of a multicrystalline silicon wafer. No special polarization settings were used for these measurements. In addition to the first-order Raman peak of silicon in the vicinity of 521 cm^{-1} (Ref. 20) there are several other peaks visible. These peaks originate from the plasma lines of the HeNe laser. As the peak positions of the plasma lines are physically fixed, they serve as a reference for the determination of the accurate frequency shifts of the silicon Raman peaks.²⁰ An accidental drift of the optical grating with time will be eliminated by correcting Raman peak positions with positions of the plasma lines.

In many cases, the stresses are too small to produce a visible lifting of degeneracy of the three optical phonon frequencies. This makes the direct determination of the three

frequency shifts $\Delta\omega_1$, $\Delta\omega_2$, and $\Delta\omega_3$ impossible. As a tempting approximation, one could assume $\Delta\omega_1 \approx \Delta\omega_2 \approx \Delta\omega_3$. However, this approach is extremely inaccurate, as the obscured frequency shifts can vary several wave numbers from each other without producing any clearly visible lifting of degeneracy. Thus, we will follow another indirect strategy to obtain the three frequency shifts $\Delta\omega_1$, $\Delta\omega_2$, and $\Delta\omega_3$ with sufficient accuracy.

Once we know the grain orientation, we are able to simulate separately the intensity variations of the three optical phonons with polarization settings. With the $\lambda/2$ plate and the two positions of the analyzer (x and y) we may define two intensity functions for each phonon: $I_j^X(\phi)$ and $I_j^Y(\phi)$ where the upper index labels the analyzer position and the lower index nominates the phonon mode (1, 2, 3 or x , y , z once the crystal axes have been identified). In total, we obtain six single intensity functions that can be converted into six intensity ratio functions, $Q_1^X(\phi)$, $Q_2^X(\phi)$, $Q_3^X(\phi)$ and $Q_1^Y(\phi)$, $Q_2^Y(\phi)$, $Q_3^Y(\phi)$:

$$Q_1^X(\phi) = \frac{I_1^X(\phi)}{I_2^X(\phi) + I_3^X(\phi)}$$

$$\text{Cycl. perm.} \rightarrow Q_2^X(\phi), Q_3^X(\phi),$$

and

$$Q_1^Y(\phi) = \frac{I_1^Y(\phi)}{I_2^Y(\phi) + I_3^Y(\phi)} \quad (20)$$

$$\text{Cycl. perm.} \rightarrow Q_2^Y(\phi), Q_3^Y(\phi).$$

The domains where the values of the above given intensity ratio functions are clearly greater than 1, e.g., at the maxima positions, define polarization settings (single-mode polarization settings) where the intensity of one phonon dominates over the sum of the intensities of the two remaining phonons. Our simulations show, that for most of the arbitrary grain orientations one can find three polarization settings, where, respectively, one of the three phonon modes clearly dominates the two other ones.

The totally measured frequency shift $\overline{\Delta\omega_T}$ of a Raman peak (lifting of degeneracy not visible) can be written as⁹

$$\overline{\Delta\omega_T} = \sum_{j=1}^3 \frac{\Delta\omega_j \cdot I_j}{I_T}. \quad (21)$$

I_T is the measured total intensity of the Raman peak, I_j are the three single intensity portions of the three phonon modes, and $\Delta\omega_j$ are the three corresponding frequency shifts.

If we find, for example, a polarization setting where one phonon mode (labeled mode 1) possesses a certain intensity ratio function of Q_1^* , then the totally measured frequency shift $\overline{\Delta\omega_T}^*$ is given in terms of Q_1^* by

$$\overline{\Delta\omega_T}^* = \frac{Q_1^*}{Q_1^* + 1} \cdot \Delta\omega_1 + \frac{1}{Q_1^* + 1} \cdot \left(\frac{I_2}{I_2 + I_3} \cdot \Delta\omega_2 + \frac{I_3}{I_2 + I_3} \cdot \Delta\omega_3 \right), \quad (22)$$

i.e., the larger a certain intensity ratio function of a phonon mode at a certain polarization setting, the higher the accu-

racy of the measured frequency shift of that particular phonon mode. If we find three polarization settings so that one of the three phonon modes dominates the two others, we may carry out three frequency shift measurements with these polarization settings. In consequence, we can assign the obtained frequency shifts mainly to the dominant modes.

This way we are able to measure the three frequency shifts $\Delta\omega_1$, $\Delta\omega_2$, and $\Delta\omega_3$ almost separately, though the lifting of degeneracy is not visible.

C. Correcting the influence of the objective lenses

We perform the stress measurements with objective lenses $50\times$ (numerical aperture 0.75) or $100\times$ (numerical aperture 0.9). These objective lenses influence the intensity functions $I_j^x(\phi)$ and $I_j^y(\phi)$ as well as the intensity ratio functions $Q_j^x(\phi)$ and $Q_j^y(\phi)$. We take into account for these influences in our calculations but do not discuss the mathematical details here as this is not the main topic of this article. In general, the consideration of the influences of the objective lenses leads to lengthy and complicated expressions for the intensity functions and the intensity ratio functions. The detailed mathematical derivations and the explicit expressions will be addressed in a forthcoming article.

D. Summary of the measurement procedure

With the three single-mode polarization settings, we perform three single Raman frequency shift mappings within the area of interest. From these three mappings we obtain the three drift corrected frequency shifts $\Delta\omega_1$, $\Delta\omega_2$, and $\Delta\omega_3$ almost separately at every measurement point of the mapping. The stress tensor components (in the reference coordinate system) can then be calculated using the following procedure:

1. We start with the assumption of an ideal plane stress state (in the reference coordinate system), e.g., we set $\Delta_z=0$ in Eq. (13). We insert the measured frequency shifts $\Delta\omega_1$, $\Delta\omega_2$, and $\Delta\omega_3$ into Eq. (13) and choose reasonable start values for the stress components σ_{xx} , τ_{xy} , and σ_{yy} and start solving the equation system Eq. (13) by iteration procedures.
2. The values of the stress components σ_{xx} , τ_{xy} , and σ_{yy} are chosen such that the norm of the residual vector in Eq. (13) assumes a minimum.
3. From the determined stress components, we reconstruct the characteristic polynomial Eq. (12) and calculate the total frequency shifts $\Delta\omega_1^*$, $\Delta\omega_2^*$, and $\Delta\omega_3^*$ from this polynomial.
4. We compare the total frequency shifts $\Delta\omega_1^*$, $\Delta\omega_2^*$, and $\Delta\omega_3^*$ of the reconstructed polynomial with the measured frequency shifts $\Delta\omega_1$, $\Delta\omega_2$, and $\Delta\omega_3$. If the reconstructed values deviate more than the peak shift resolution of $\pm 0.05 \text{ cm}^{-1}$ from the measured frequency shifts, the value of Δ_z in Eqs. (13) has to be slightly changed from $\Delta_z=0$ to $\Delta_z \neq 0$ (e.g., the stress components with a z direction cannot be neglected anymore) until the de-

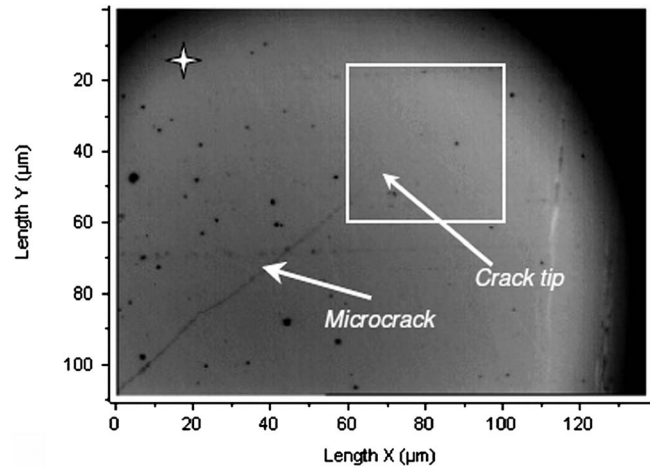


FIG. 3. Micrograph of the surface of a silicon grain containing a microcrack. The grain orientation will be determined at the position that is marked with a cross. We assume that this position will not be affected too much by the stress field around the tip of the microcrack. The 40×40 measuring points were used for the stress mappings.

viations of the measured frequency shifts from the reconstructed values become smaller than the peak shift resolution.

E. Examples

Stress measurements on multicrystalline solar cell material are of technological importance since stresses and electro-optical performance interdepend as well as fracture of multicrystalline solar cells is already a problem in practice. This is true, especially since the thickness of the multicrystalline solar cell wafers will further shrink in future and thus the material will tend to be increasingly prone to fracture.

1. The stress state at the tip of a microcrack

Figure 3 shows an optical micrograph of the surface of an arbitrarily oriented grain of a multicrystalline solar silicon wafer. The grain contains a microcrack. We expect the highest stresses at the tip of the microcrack. As high stresses influence the Raman tensors, the intensities of the Raman bands will also be influenced by high stresses, i.e., Eq. (3) that is used to determine the crystallographic orientation from intensity measurements is affected when high stresses occur. Therefore, we measure the grain orientation at a position that is not affected too much by the stress field around the tip of the microcrack. In Fig. 3 this position is marked with a white cross. The white rectangle indicates the area close to the crack tip that was stress mapped.

Figure 4 shows the intensity variations with the polarization direction ϕ of the incident light beam, measured at the location marked with the white cross in Fig. 3. The two curves belong to the x - and the y -analyzer position, respectively. The mean values of the two intensity curves differ, as the optical grating influences the intensities of the x - and y -scattered light in a different way [correction factor m , see Eq. (15)]. As we already discussed, this has no implications on the determination of the crystallographic orientations.

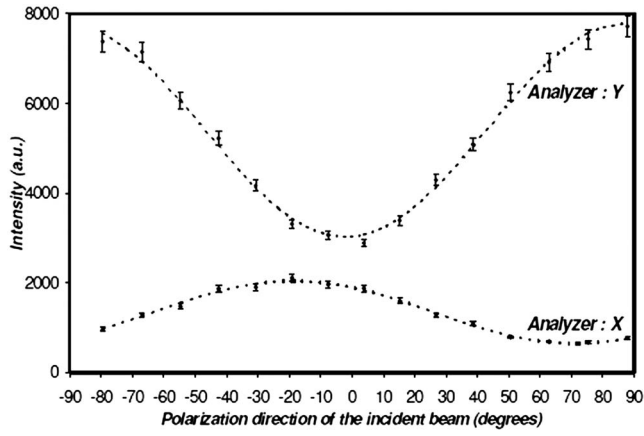


FIG. 4. Variations of the Raman intensities with the polarization direction of the incident beam for the x- and y- analyzer positions. The dashed curves represent the best fit functions Fit_{ϕ_x} and Fit_{ϕ_y} of Eqs. (18).

The error bars account for the $\sim 3\%$ -intensity variations of the incident laser light. The dashed curves in Fig. 4 represent the best fit functions Fit_{ϕ_x} and Fit_{ϕ_y} . From these two fit functions, we obtain the following three Euler-angles:

$$\alpha = 51^\circ \pm 2^\circ, \quad \beta = 69^\circ \pm 2^\circ, \quad \gamma = 56^\circ \pm 2^\circ,$$

with a norm of the residual vector of 1.6145×10^{-3} . The error of 2° results mainly from the variation of the laser intensity.

These three Euler angles give the following rotation matrix:

$$\mathbf{T}(\alpha, \beta, \gamma) = \begin{pmatrix} 0.122 & -0.678 & 0.725 \\ 0.623 & -0.516 & -0.587 \\ 0.773 & 0.524 & 0.359 \end{pmatrix}.$$

Figure 5 shows the six simulated ratio functions $Q_j^X(\phi)$ and $Q_j^Y(\phi)$ for the above determined rotation matrix and the $50\times$ objective lens.

The simulations of the six ratio functions $Q_j^X(\phi)$ and $Q_j^Y(\phi)$, shown in Fig. 5, for the orientation of the silicon grain containing the microcrack, suggest that we use the following three polarization settings, as given by the polarization direction of the incident laser light and the analyzer position, for the separate measurements of the three frequency shifts $\Delta\omega_1$, $\Delta\omega_2$, and $\Delta\omega_3$:

$$\Delta\omega_1(\text{Phonon 1}): (19^\circ, X),$$

$$\Delta\omega_2(\text{Phonon 2}): (28^\circ, Y),$$

$$\Delta\omega_3(\text{Phonon 3}): (-27^\circ, Y).$$

The area labeled with the rectangle in Fig. 3 was mapped with the three polarization settings for $\Delta\omega_j$ using 40×40 measuring points, respectively. The peaks of the first-order silicon Raman band and the peaks of the reference plasma line were fitted with a Gaussian/Lorentzian fit function. The three mappings of the three corresponding frequency shifts $\Delta\omega_1$, $\Delta\omega_2$, and $\Delta\omega_3$ are shown in Figs. 6(a)–6(c). We correlate each of the three frequency shifts, that are used to locally determine the components of the stress tensors close to the crack tip, to a reference point (upper left corner in the map-

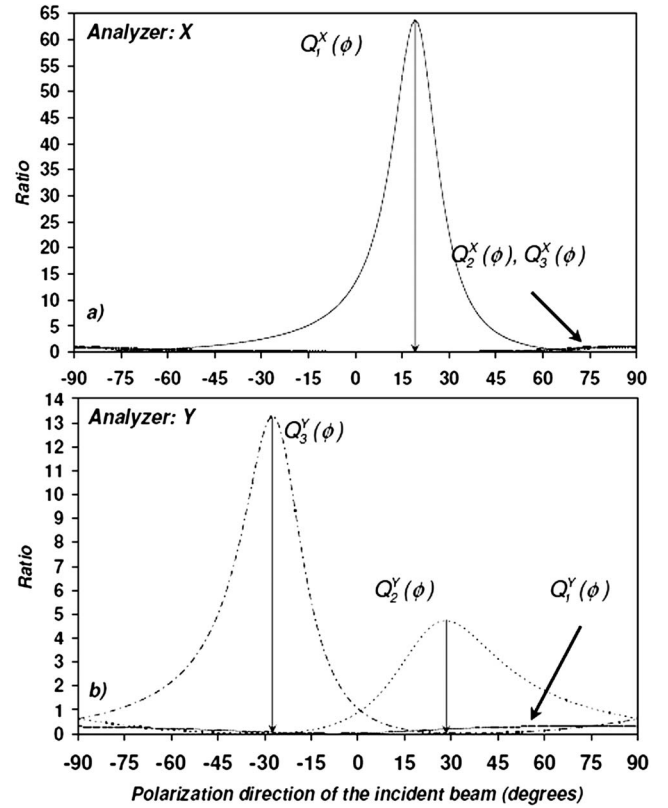


FIG. 5. Simulation of the six intensity ratio functions $Q_j^X(\phi)$ (a) and $Q_j^Y(\phi)$ (b). The marked maximum positions indicate the polarization settings where the intensity of one of the three phonon modes dominates over the intensity sum of the two remaining phonons.

pings, as indicated in Fig. 6 by an arrow). This procedure will eliminate peak shifts due to optical artifacts, i.e., the calculated stress tensors refer to the stress state at the labeled reference point. This is possible due to the fact that the solutions of Eqs. (13) linearly depend on the frequency shifts

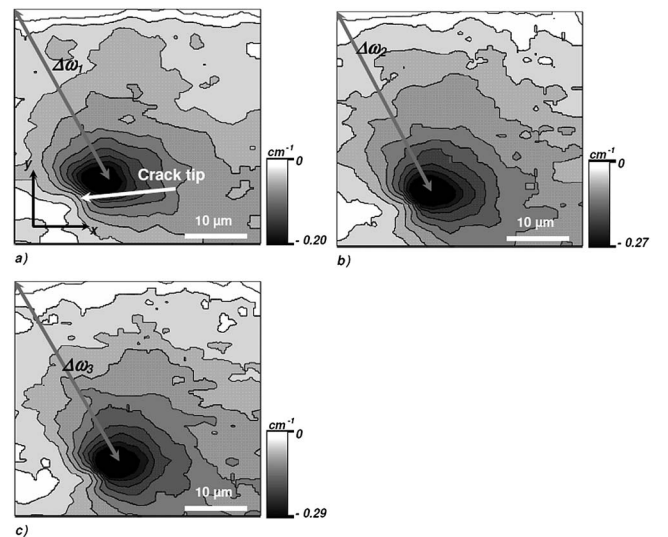


FIG. 6. Three mappings of the Raman frequency shifts close to the crack tip (area marked with a rectangle in Fig. 3). The three mappings correspond to the three polarization settings $\Delta\omega_1$ (19° ; X), $\Delta\omega_2$ (28° ; Y), and $\Delta\omega_3$ (-27° ; Y). The values of the frequency shifts in the upper left corners of the mappings are used as references for the frequency shift distributions given by the gray scales. The mappings have been graphically interpolated for better visibility.

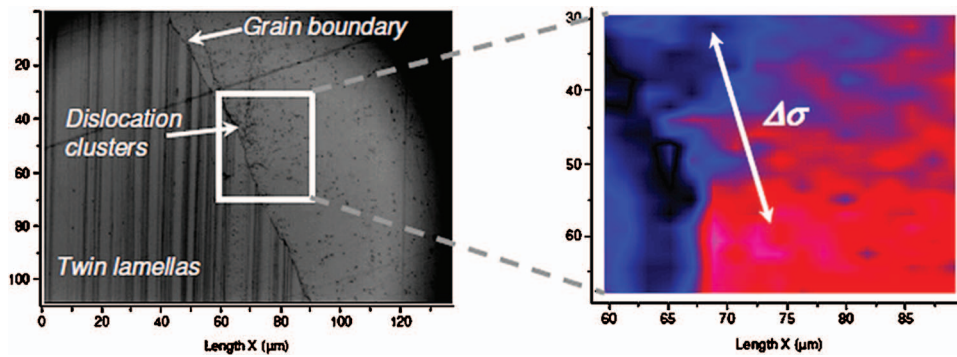


FIG. 7. (Color) Light optical micrograph (left) of a surface of a polycrystalline silicon wafer for photovoltaic applications. The micrograph shows a grain boundary which separates a region of twin lamellas from an arbitrarily oriented grain. Close to the grain boundary fan-shaped dislocation clusters are found. A mapping (right) of the Raman frequency shifts reveals a stress field close to the grain boundary which seems to correlate with the dislocation clusters. A detailed analysis of the Raman frequency shifts, taking into account the crystal orientation, yields the following difference stress tensor referring to the reference coordinate system (white arrow; red color depicts relative compressive stresses):

$$\Delta\sigma = \begin{pmatrix} -59 \pm 13 & -14 \pm 5 & 0 \\ -14 \pm 5 & -68 \pm 15 & 0 \\ 0 & 0 & -13 \pm 5 \end{pmatrix} \text{ MPa.}$$

$\Delta\omega_j$. That is, if we measure, for example, at a position 1 the frequency shift set $(\Delta\omega_1^{(1)}, \Delta\omega_2^{(1)}, \Delta\omega_3^{(1)})$ that leads to the stress tensor $\sigma^{(1)}$ as the best solution for Eqs. (13) and if we measure at position 2 the set $(\Delta\omega_1^{(2)}, \Delta\omega_2^{(2)}, \Delta\omega_3^{(2)})$ that yields $\sigma^{(2)}$ as the best solution for Eqs. (13), then the difference stress tensor $\Delta\sigma = (\sigma^{(2)} - \sigma^{(1)})$ is the best solution of Eq. (15) if we insert the difference frequency shift set $(\Delta\omega_1^{(2)} - \Delta\omega_1^{(1)}, \Delta\omega_2^{(2)} - \Delta\omega_2^{(1)}, \Delta\omega_3^{(2)} - \Delta\omega_3^{(1)})$ into Eq. (13). A superimposed long range stress field, which may also be present in the grains, is eliminated this way. Following this procedure we can now determine the difference stress tensor $\Delta\sigma$ (referring to the reference coordinate system shown in Fig. 6) from the measured frequency shift differences $\Delta\omega_1 = -0.20 \text{ cm}^{-1}$, $\Delta\omega_2 = -0.27 \text{ cm}^{-1}$, and $\Delta\omega_3 = -0.29 \text{ cm}^{-1}$ (for simplicity we write here $\Delta\omega_j$ for the positional differences $\Delta\omega_j^{(2)} - \Delta\omega_j^{(1)}$).

At first, we try to solve Eqs. (13) with the above given frequency shift differences $\Delta\omega_j$ by setting $\Delta\epsilon_z = 0$.

The best numerical solution of Eq. (13) then yields a difference stress tensor of

$$\Delta\sigma = \begin{pmatrix} 69 & -11 & 0 \\ -11 & 67 & 0 \\ 0 & 0 & 0 \end{pmatrix} \text{ MPa.}$$

However, the numerical procedure to solve the equation system (13) yields a solution with a large norm of the residual vector for our three frequency shifts. Reconstruction of the characteristic polynomial (12) from the above given stress components yields the following reconstructed values:

$$\Delta\omega_1^* = -0.08 \text{ cm}^{-1}, \quad \Delta\omega_2^* = -0.32 \text{ cm}^{-1},$$

$$\Delta\omega_3^* = -0.40 \text{ cm}^{-1},$$

i.e., the deviations of the first and third reconstructed root from the measured frequency shift differences are larger than the peak shift resolution of $\pm 0.05 \text{ cm}^{-1}$. We therefore increase the value of $\Delta\epsilon_z$ in Eqs. (13) to account for the residual stress components in the z direction, which also influence the

frequency shifts. We then finally obtain a difference stress tensor of

$$\Delta\sigma = \begin{pmatrix} 57 \pm 12 & -7 \pm 3 & 0 \\ -7 \pm 3 & 54 \pm 11 & 0 \\ 0 & 0 & 19 \pm 4 \end{pmatrix} \text{ MPa.}$$

The given errors account for the limited peak shift resolution of $\pm 0.05 \text{ cm}^{-1}$ and the uncertainty of the measurement of the crystal orientation. The reconstructed values using the above given stress components now deviate less than $\pm 0.05 \text{ cm}^{-1}$ from the measured frequency shifts.

The obtained stress tensor is quite reasonable: As expected from theory,²¹ the stress state around the crack tip is tensile and the stress components lie within the anticipated range. Regarding the position of the crack (the crack comprises an angle of $\approx 45^\circ$ with the axes of the reference coordinate system) and the approximately symmetric stress field around the crack tip, it is plausible, that $\Delta\sigma_{xx} \approx \Delta\sigma_{yy}$.

2. Stress fields at grain boundaries

Inhomogeneous stress distributions can often be found close to grain boundaries in polycrystalline silicon wafers. The local stress gradients are produced by the inhomogeneous temperature gradients within the ingot during the cooling process. The stress fields close to grain boundaries are critical in terms of the mechanical stability of the wafer, as they can act as sources for crack formation if additional external stress is applied. With μ -Raman spectroscopy we are able to detect such stress fields and determine stress-tensor gradients on a length scale of a few microns, as exemplified with Fig. 7. The determination of the stress components follows the procedure described above. In many cases, the stress gradients close to grain boundaries are accompanied by fan-shaped dislocation clusters, which seem to emanate from the grain boundaries. The light optical micrograph in Fig. 7 shows an example of these features. The dislocation clusters might form during the solidification process to relieve stresses. Therefore, the stress fields we measure with

μ -Raman spectroscopy are the remaining stress fields that could not be reduced by dislocation formation. A detailed investigation of the stress fields close to these dislocation clusters will be presented in a forthcoming article.

IV. CONCLUSIVE DISCUSSION

This paper provides a Raman spectroscopy based analytic procedure to study stress/strain distributions in polycrystalline silicon solar cell materials. Since stress measurements depend on orientation, a combined orientation and stress analysis by Raman spectroscopy is needed. This article provides it for the first time. This surely has implications on a wider use of this technique which is nondestructive, relatively fast, and reliable without the need for special sample preparation.

In what is needed is a Raman spectroscopy setup, equipped with a polarizer and analyzer. The wavelength used determines the information depth and the probed volume. Based on our stress measurements we can state the following:

1. Stresses close to the theoretical strength of bulk silicon are locally assumed at structures like grain boundary

triple points, points of origin of dislocation clusters, silicon/metal interfaces, etc., and close to microcracks. This is truly a problem in view of the targeted decrease of wafer thickness in photovoltaics.

2. Stresses are inhomogeneously distributed with maximum values of the order of ~ 500 MPa.
3. The sensitivity of the method is ~ 15 MPa. The lateral resolution is of the order of $1 \mu\text{m}$. Enhancement of lateral resolution may be possible by tip enhanced Raman spectroscopy (TERS).^{22,23}

ACKNOWLEDGMENTS

This work has been performed within the project ASIS (Alternative Silicon for Solar Cells) granted by the Federal Ministry of Environment, Preservation and Reactor Safety (Bundesministerium für Umwelt, Naturschutz und Reaktorsicherheit, BMU), Berlin, Germany (No. 0329846G).

APPENDIX

The crystallographic grain orientation is based on the explicit expressions for the functions $f_{ij}(\alpha, \beta, \gamma)$ in Eq. (16). For the rotation matrix, we write

$$\mathbf{T}(\alpha, \beta, \gamma) = \begin{pmatrix} t_{11} & t_{12} & t_{13} \\ t_{21} & t_{22} & t_{23} \\ t_{31} & t_{32} & t_{33} \end{pmatrix} = \begin{pmatrix} \cos \alpha \cos \gamma - \cos \beta \sin \gamma \sin \alpha & -\cos \alpha \sin \gamma - \cos \beta \cos \gamma \sin \alpha & \sin \beta \sin \alpha \\ \sin \alpha \cos \gamma + \cos \beta \sin \gamma \cos \alpha & -\sin \alpha \sin \gamma + \cos \beta \cos \gamma \cos \alpha & -\sin \beta \cos \alpha \\ \sin \gamma \sin \beta & \cos \gamma \sin \beta & \cos \beta \end{pmatrix}. \quad (\text{A1})$$

Then the functions $f_{ij}(\alpha, \beta, \gamma)$ become

$$\begin{aligned} f_{11}(\alpha, \beta, \gamma) &= 4[(t_{11} \cdot t_{21})^2 + (t_{11} \cdot t_{31})^2 + (t_{31} \cdot t_{21})^2], \\ f_{12}(\alpha, \beta, \gamma) &= 4 \cdot \{t_{11} \cdot t_{21} \cdot (t_{11} \cdot t_{22} + t_{12} \cdot t_{21}) + t_{11} \cdot t_{31} \cdot (t_{11} \cdot t_{32} + t_{12} \cdot t_{31}) + t_{31} \cdot t_{21} \cdot (t_{21} \cdot t_{32} + t_{22} \cdot t_{31})\}, \\ f_{13}(\alpha, \beta, \gamma) &= (t_{11} \cdot t_{22} + t_{12} \cdot t_{21})^2 + (t_{21} \cdot t_{32} + t_{22} \cdot t_{31})^2 + (t_{11} \cdot t_{32} + t_{12} \cdot t_{31})^2, \\ f_{22}(\alpha, \beta, \gamma) &= 2 \cdot (t_{12})^2 \cdot \{(t_{21})^2 + (t_{31})^2\} + 2 \cdot (t_{11})^2 \cdot \{(t_{22})^2 + (t_{32})^2\} + 2 \cdot \{(t_{32})^2 \cdot (t_{21})^2 + (t_{22})^2 \cdot (t_{31})^2\} \\ &\quad + 12 \cdot t_{11} \cdot t_{12} \cdot \{t_{31} \cdot t_{32} + t_{21} \cdot t_{22}\} + 12 \cdot t_{31} \cdot t_{21} \cdot t_{32} \cdot t_{22}, \\ f_{23}(\alpha, \beta, \gamma) &= 4 \cdot \{t_{12} \cdot t_{11} \cdot (t_{32})^2 + t_{31} \cdot t_{32} \cdot (t_{12})^2 + t_{21} \cdot t_{22} \cdot (t_{32})^2 + t_{31} \cdot t_{32} \cdot (t_{22})^2 + t_{11} \cdot t_{12} \cdot (t_{22})^2 + t_{21} \cdot t_{22} \cdot (t_{22})^2\}, \\ f_{33}(\alpha, \beta, \gamma) &= 4 \cdot \{(t_{12} \cdot t_{22})^2 + (t_{12} \cdot t_{32})^2 + (t_{22} \cdot t_{32})^2\}. \end{aligned} \quad (\text{A2})$$

A. Relevant material parameters of silicon

Phonon Deformation Potentials (PDP's)²⁴:

$$p/(\omega_0)^2 = -1.85 \pm 0.06, \quad q/(\omega_0)^2 = -2.31 \pm 0.06, \quad r/(\omega_0)^2 = -0.71 \pm 0.02,$$

$$\omega_0 = 521 \text{ cm}^{-1}.$$

Elastic compliance constants²⁵:

$$S_{11} = 7.67 \times 10^{-12} \text{ Pa}^{-1}, \quad S_{12} = -2.134 \times 10^{-12} \text{ Pa}^{-1},$$

$$S_{44} = 12.5 \times 10^{-12} \text{ Pa}^{-1}.$$

Refraction index of silicon at 633 nm (Ref. 26):

$$n = 3.87.$$

- ¹I. De Wolf, H. E. Maes, and S. K. Jones, J. Appl. Phys. **79**, 7148 (1996).
- ²I. De Wolf, Semicond. Sci. Technol. **11**, 139 (1996).
- ³I. De Wolf, J. Raman Spectrosc. **30**, 877 (1999).
- ⁴J. Michler, Y. V. Kaenel, J. Stiegler, and E. Blank, J. Appl. Phys. **83**, 187 (1998).
- ⁵B. Dietrich and K. F. Dombrowski, J. Raman Spectrosc. **30**, 893 (1999).
- ⁶E. Bonera, M. Fanciulli, and D. N. Batchelder, Appl. Phys. Lett. **81**, 3377 (2002).
- ⁷E. Bonera, M. Fanciulli, and D. N. Batchelder, J. Appl. Phys. **94**, 2729 (2003).
- ⁸P. Puech, S. Pinel, R. G. Jasinevicius, and P. S. Pizani, J. Appl. Phys. **88**, 4582 (2000).
- ⁹S. Narayanan, S. R. Kalidindi, and L. S. Schadler, J. Appl. Phys. **82**, 2595 (1997).
- ¹⁰G. H. Loechelt, N. G. Cave, and J. Menendez, J. Appl. Phys. **86**, 6164 (1999).
- ¹¹S. D. Brotherton, J. R. Ayres, M. J. Edwards, C. A. Fisher, C. Glaister, J. P. Gowers, D. J. McCulloch, and M. Trainor, Thin Solid Films **337**, 188 (1999).
- ¹²R. Loudon, Adv. Phys. **13**, 423 (1964).
- ¹³K. Mizoguchi and S. Nakashima, J. Appl. Phys. **65**, 2583 (1989).
- ¹⁴P. Y. Yu and M. Cardona, *Fundamentals of Semiconductors* (Springer, Berlin, 1996).
- ¹⁵S. Ganesan, A. A. Maradudin, and J. Oitmaa, Ann. Phys. **56**, 556 (1970).
- ¹⁶T. Ito, H. Azuma, and S. Noda, Jpn. J. Appl. Phys. **33**, 171 (1994).
- ¹⁷F. Secco, D' Aragona, J. Electrochem. Soc. **119**, 948 (1972).
- ¹⁸J. B. Hopkins and L. A. Farrow, J. Appl. Phys. **59**, 1103 (1986).
- ¹⁹J. J. More, B. S. Garbow, and K. E. Hillstrom, User Guide to MINPACK, Argonne National Laboratory Report ANL-80-74 (1980).
- ²⁰I. De Wolf, J. Jimenez, J. Landesman, C. Frigeri, P. Braun, E. Da Silva, and E. Calvet, *New Developments in Optical Spectroscopy for the Characterization of Semiconductor Devices (Nostradamus)* (European Commission, Brussels, 1998).
- ²¹T. L. Anderson, *Fracture Mechanics: Fundamentals and Applications* (Taylor & Francis, London, 2004).
- ²²B. Pettinger, B. Ren, G. Picardi, R. Schuster, and G. Ertl, Phys. Rev. Lett. **92**, 096101 (2004).
- ²³W. X. Sun and Z. X. Chen, J. Raman Spectrosc. **34**, 668 (2003).
- ²⁴E. Anastassakis, A. Cantarero, and M. Cardona, Phys. Rev. B **41**, 7529 (1990).
- ²⁵W. A. Brantley, J. Appl. Phys. **44**, 534 (1973).
- ²⁶H. R. Philipp and E. A. Taft, Phys. Rev. **120**, 37 (1960).